Direct numerical simulations of multiple swirling jets issued into a crossflow

Tomoaki Watanabe (渡邉 智昭),[1, a)] Takahiko Nishizaki (西崎 貴彦),[2] Tsukuru Furuta (古田 作),[2] and Koji Nagata (長田 孝二)[1]

[1)] *Department of Mechanical Engineering and Science, Kyoto University, Kyoto 615-8530, Japan*

[2)] *Department of Aerospace Engineering, Nagoya University, Nagoya 464-8603, Japan*

(Dated: 21 July 2025)

A jet in crossflow (JICF) is a canonical configuration widely studied in fluid mechanics. In this study, direct numerical simulations were conducted to investigate the flow and scalar transport characteristics of multiple slightly heated swirling JICFs. The simulations spanned a range of swirl numbers ($Sw = 0$–0.6) at a fixed jet Reynolds number of 2100 and a jet–crossflow velocity ratio of 3.3. A total of 15 jets were arranged in three rows along the streamwise direction and five columns in the spanwise direction, with periodicity assumed in the spanwise direction. The results indicate that moderate swirl ($Sw = 0.2$–0.4) enhances reverse flow near the wall, reduces jet height, and promotes the formation of a spanwise mean flow. Notably, strong swirl ($Sw = 0.6$) leads to a rapid collapse of the jet potential core and significantly limits jet penetration into the crossflow. These swirl effects cause high-temperature fluid from the jets to remain near the wall in the downstream region. The resulting modifications to the mean flow lead to the enhanced production of turbulent kinetic energy in moderate swirl cases, generating large velocity fluctuations that persist further downstream. A scaling analysis of the energy dissipation rate reveals the presence of non-equilibrium turbulence, where the non-dimensional dissipation rate C_ε scales inversely with the turbulent Reynolds number. Further downstream, C_ε approaches a constant, thus indicating a transition to an equilibrium state of energy cascade. These findings provide novel insights into the role of swirl in modifying jet dynamics, turbulence, and scalar transport in JICF configurations.

[a)] Author to whom correspondence should be addressed: watanabe.tomoaki.8x@kyoto-u.ac.jp

I. INTRODUCTION

A jet issuing perpendicularly into a mainstream, commonly referred to as a jet in crossflow (JICF),[1] is a canonical configuration that appears in various engineering applications, including fuel injection in gas turbine combustors and the dispersion of exhaust plumes. Notably, the aforementioned examples have motivated extensive research on the JICF configuration. The complex vortex structures formed by the interaction between the jet and the crossflow are strongly influenced by various parameters, including the velocity ratio between the jet and the mainstream, the momentum flux ratio, the jet orifice geometry, and the Reynolds number.[2,3] In the near field of the jet, four characteristic coherent vortex structures are typically observed: the jet shear layer vortex, the counter-rotating vortex pair (CVP), the horseshoe vortex, and the wake vortex.[2,4–8] These structures are important in the flow evolution downstream of the jet inlet, as well as in the mixing processes of heat and species concentrations.[9]

In practical engineering applications, complex flow behaviors often emerge due to the interplay between jet and mainstream conditions. A notable example is the airflow dynamics of air-cooled heat exchangers used in industrial plants.[10] In such systems, multiple swirling jets discharged from the heat exchangers interact with the ambient atmospheric flow above the facility. This interaction can cause the hot jets to deflect horizontally and become entrained back into the heat exchanger intakes, leading to a significant increase in intake air temperature and a consequent reduction in thermal efficiency.[11–13] This phenomenon, known as hot air recirculation (HAR), poses a critical challenge in plant engineering and has been the subject of extensive studies to understand and mitigate its impact on system performance.

The aforementioned example of flow discharged from heat exchangers can be modeled in canonical JICF configurations as multiple swirling flows issued from a jet array into a mainstream. Despite the practical importance of this configuration, it has rarely been investigated in previous studies, which have instead focused on either a single swirling jet or multiple jets without swirling motions into a mainstream. Previous studies have demonstrated that swirl can significantly affect the symmetry and trajectory of CVPs in a single jet issued into a main flow. Denev et al. conducted (large eddy simulations) LESs of a swirling JICF and investigated the effects of swirl on coherent vortex structures.[14] Their analysis revealed that the presence of swirl induces significant asymmetry in the flow, such

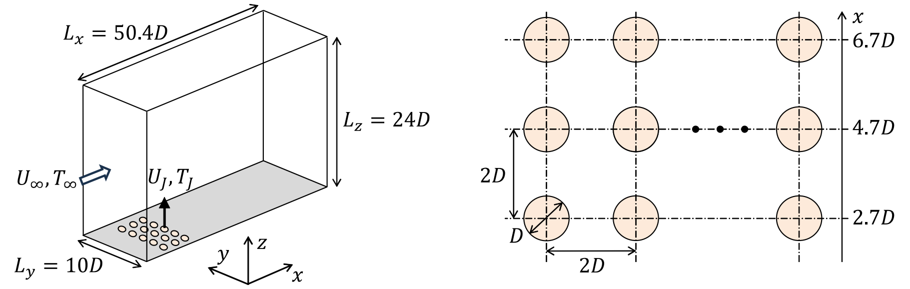

FIG. 1. Direct numerical simulation of multiple jets issued into a crossflow.

as shifting one of the counter-rotating vortices closer to the wall. Regarding jet arrays, previous investigations have examined configurations in which multiple jets are arranged in the streamwise direction[15–17] and spanwise direction.[18–20] Another study also investigated the interaction of multiple jets and cylinders in a crossflow.[21] Collectively, these studies suggest that the blocking effect of upstream jets can significantly alter the downstream flow field. For example, CVPs from twin jets separated in the spanwise direction interact and rapidly merge when the jet separation distance is small.[18] However, jet arrays arranged in both the streamwise and spanwise directions have not yet been systematically investigated, despite being more representative of practical applications. Moreover, the impact of swirl in such multi-jet configurations remains largely unexplored.

To build on the current understanding of swirling JICFs, we conducted direct numerical simulations (DNSs) of multiple swirling jets to elucidate how swirl and jet interactions influence flow evolution and passive scalar transport, with a focus on far-field turbulence characteristics. We demonstrate that swirling motions enhance the blocking effects of the jets, leading to the suppression of vertical scalar transport. The interaction of the swirling jets also leads to the formation of large-scale spanwise flow. The influences of swirl motions on the mean flow and scalar profiles, as well as the turbulent kinetic energy, were also explored using the DNS data.

II. DNSS OF SWIRLING JETS ISSUED INTO A CROSSFLOW

A. Swirling jets issued into a crossflow

DNS was conducted for jets with and without swirl issued into a crossflow. Figure 1 presents a schematic of the flow setup. The mainstream, spanwise, and vertical directions are denoted by x, y, and z, respectively. The corresponding velocity components are u, v, and w. The crossflow velocity is U_∞, the jet diameter is D, and the bulk jet velocity in the vertical direction is U_J. The DNS also includes heat transfer arising from the temperature difference between the crossflow and the jet, $T_0 = T_J - T_\infty$ with $T_J > T_\infty$. It is assumed that T_0 is small enough to treat temperature as a passive scalar since buoyancy effects are negligible for small T_0 values. The temperature deviation from T_∞ is denoted by T.

The governing equations are the Navier–Stokes equations and the temperature transport equation for incompressible fluid, written as

$$\frac{\partial u_j}{\partial x_j} = 0, \tag{1}$$

$$\frac{\partial u_i}{\partial t} + \frac{\partial u_i u_j}{\partial x_j} = -\frac{1}{\rho}\frac{\partial p}{\partial x_i} + \nu \frac{\partial^2 u_i}{\partial x_j \partial x_j}, \tag{2}$$

$$\frac{\partial T}{\partial t} + \frac{\partial u_j T}{\partial x_j} = \alpha \frac{\partial^2 T}{\partial x_j \partial x_j}, \tag{3}$$

where t denotes time, x_i is the position, u_i is the velocity vector, ρ is the constant density, p is the pressure, ν is the kinematic viscosity, and α is the thermal diffusivity. The Reynolds number is defined as $Re = U_\infty D/\nu$, and the Prandtl number is defined as $Pr = \nu/\alpha$. The DNS was conducted for $Re = 6930$, $Pr = 1$, and a velocity ratio of $U_J/U_\infty = 3.3$ under different swirl conditions. For these values of Re and U_J/U_∞, the jet Reynolds number $Re_J = U_J D/\nu$ was 2100. These conditions were chosen to enable comparisons with previous studies, as detailed in the Appendix, where the DNS of a single JICF is compared with other numerical results. For each flow condition, time was advanced until $t = 200(D/U_\infty)$.

An overview of the computational domain is presented in Fig. 1. The domain dimensions were set to $(L_x, L_y, L_z) = (50.4D, 10D, 24D)$. The coordinate origin was located at the bottom corner of the computational domain. A total of 15 jets were arranged in three rows in the x direction and five columns in the y direction. The spacing between adjacent jet centers was $2D$, and the coordinates of the jet centers were specified as $x = 2.7D, 4.7D, 6.7D$

and $y = 1D, 3D, 5D, 7D, 9D$. The spacing of $2D$ was chosen as a representative case based on the design of some air-cooled heat exchangers discussed in the introduction. The initial velocity field was set to a uniform flow, $(u, v, w) = (U_\infty, 0, 0)$. At the inflow boundary of the crossflow, the velocity was specified as $(u, v, w) = (U_\infty, 0, 0)$ for $y/D_0 > 0.5$, while below this height, a boundary layer velocity profile was applied following Ref. 22. The temperature at the initial condition and inflow boundary was set to $T = 0$. A convective outflow condition[23] was applied at the outflow boundary. Periodic boundary conditions were imposed in the spanwise direction, assuming that the jet array is infinitely large in this direction. A no-slip condition with $\partial T/\partial z = 0$ was imposed at the bottom boundary, and a slip condition was applied at the top boundary. Some previous numerical studies have adopted a computational domain that includes a straight pipe from which a jet is issued into a crossflow, in order to capture the interaction between the crossflow and the internal pipe flow.[14] In the present study, the pipe was excluded from the computational domain since the primary focus is on the effects of swirl in multiple jets within the crossflow, rather than on detailed flow features at the jet exit. As discussed in Sec. III, the swirl effects observed in the present DNS are consistent with those reported for a single jet in LES studies that incorporated the pipe,[14] thus confirming that the simulations of the present study accurately capture the influence of swirl.

The present study adopted a simplified configuration in which 15 jets were arranged in three streamwise rows and five spanwise columns, with periodic boundary conditions imposed in the spanwise direction. This setup was chosen to investigate the effects of swirling motion in a flow configuration relevant to HAR scenarios, as discussed in Sec. I. In the context of industrial air-cooled heat exchangers, this arrangement corresponds to a repeating unit of fan arrays, which typically exhibit a large aspect ratio in the horizontal plane.[24–26] The assumption of spanwise periodicity implies that the simulated jet flow approximates the flow generated by central fan-columns in such heat exchangers. However, the current numerical setup does not fully replicate more realistic operating conditions. For example, it omits buoyancy effects and the structural elements of heat exchangers that draw in ambient air from the sides and exhaust heated air vertically. Moreover, in actual systems, the flow rate induced by individual fans may vary due to the influence of the surrounding environment. The pipe regions located below the lower computational boundary are also excluded. Although crossflow may partially enter these pipe regions and modify the jet inflow profile,

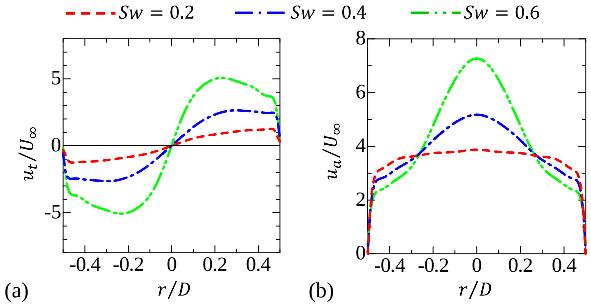

FIG. 2. Radial distributions of (a) tangential and (b) axial velocities applied as boundary conditions for swirling jets.

DNS of a single JICF suggests that this effect has only a minor influence on downstream flow development. As discussed in Sec. III, swirl-induced modifications of the initial jet, such as the shortening of the potential core and its rapid collapse, are consistent with existing numerical studies that included the internal pipe region. These agreements support the validity of the present configuration for isolating and understanding the fundamental effects of swirl in JICF systems. The jet Reynolds number of 2100 used in the present study is moderately high, albeit lower than values typically observed in heat exchanger applications. Existing studies have shown that fully developed turbulent jets (i.e., in the downstream region far from the nozzle) exhibit similar statistical properties for $Re_J \approx 2000$ and higher values, whereas Reynolds number dependence becomes more evident in the developing region where the jet transitions from laminar to turbulent.[27–29] At even lower Re_J, this dependence becomes more pronounced, even in the fully developed region.[30] Therefore, similar statistical behaviors can be expected at higher Re_J in the downstream region, where each jet has transitioned to turbulence and the jets have merged.

A non-dimensional parameter representing swirl intensity is the swirl number, which is defined as the ratio of angular momentum flux to axial momentum flux.[14] The swirl number is given by

$$Sw = \frac{\int_0^{D/2} \rho r u_t u_a \, 2\pi r \, dr}{(D/2) \int_0^{D/2} \rho u_a^2 \, 2\pi r \;\; dr}, \tag{4}$$

where $u_t(r)$ and $u_a(r)$ denote the tangential and axial velocity components of the jet, respectively, and r is the radial distance from the jet center. In this study, simulations were

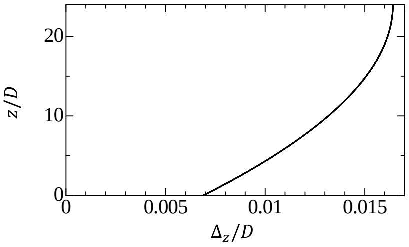

FIG. 3. Vertical distribution of vertical grid spacing Δ_z.

conducted for four Sw conditions: $Sw = 0, 0.2, 0.4$, and 0.6. Figure 2 presents the radial distributions of u_t and u_a applied as inflow boundary conditions for the swirling jets. The velocity profiles for the swirl cases were taken from those of an internal swirling flow, which have also been adopted in previous studies on swirling jets.[14] The central axial velocity increases with Sw due to the stabilizing effect arising from rotation. For non-swirling jets, the one-seventh power law of pipe flow is adopted for the axial velocity, while the tangential velocity component is set to zero.

B. Numerical methods

An in-house finite difference code based on the fractional step method was used to solve the governing equations. Spatial discretization employed a second-order fully conservative central difference scheme,[31], while temporal discretization used a third-order Runge–Kutta scheme. The BiCGStab method was employed to solve the Poisson equation for pressure. This code has been used in our earlier studies on turbulence generated by the breakdown of internal gravity waves,[32] jets,[33,34] mixing layers,[35–37] boundary layers,[38,39], and grid turbulence.[40,41] These studies have validated the code through comparisons with experiments and other DNS results.

The computational domain was discretized using regular grids. The number of grid points was set to $(N_x, N_y, N_z) = (4080, 800, 1920)$. Non-uniform grids were applied in the z direction to provide finer resolution near the bottom boundary, while uniform grids were used in the x and y directions. The grid point positions $(x(i), y(j), z(k))$ are defined using integers

$(i, j, k) = (1, ..., N_x, 1, ..., N_y, 1, ..., N_z)$ as follows:

$$x(i) = \Delta_x i, \quad y(j) = \Delta_y j, \quad z(k) = \frac{L_z}{\tanh(\alpha_z)}\left[\tanh(\alpha_z)\left(1 - \frac{k}{N_z}\right)\right] + L_z, \tag{5}$$

where $\alpha_z = 1$ is a constant controlling the grid distribution, and $\Delta_x = L_x/N_x$ and $\Delta_y = L_y/N_y$ are the grid spacings in the x and y directions, respectively. The function used to determine the grid position in the z direction is identical to that used in previous studies of boundary layers.[38,39,42,43] Figure 3 shows the distribution of the vertical grid spacing $\Delta_z(z)$, which increases with height from the bottom wall. In the other directions, the grid spacing was $\Delta_x \approx \Delta_y \approx 0.12D$. The turbulent jet did not reach $z \gtrsim 15D$. In the jet region, the grid spacing was smaller than 1.5 times the Kolmogorov scale, thereby ensuring that small-scale turbulent motions were resolved with the current grid setting. The time increment was determined using a constant Courant number of 0.5.

The statistics of flow variables were evaluated using time averages taken after $t = 100(D/U_J)$, such that the averages were taken after the flow had reached a statistically steady state. Since the jets were equidistantly spaced in the y direction with periodic boundaries, ensemble averages over the five jet columns were also taken to improve statistical convergence. Additionally, the turbulent jets became statistically homogeneous in the spanwise direction in the downstream region, where spanwise averages were used to further improve statistical convergence. The average of a quantity f is denoted by $\langle f \rangle$, while fluctuations are defined as $f' = f - \langle f \rangle$. The root-mean-square (rms) value of fluctuations was evaluated as $f_{rms} = \langle f'^2 \rangle^{1/2}$.

III. RESULTS AND DISCUSSION

A. Instantaneous flow field

Figure 4 visualizes the instantaneous streamwise velocity on an xz plane at $y = 5D$, which crosses the jet centers, for all Sw cases. The jets were inclined in the streamwise direction by the crossflow. As the jets issued from the bottom wall developed into a turbulent state, they merged, and the velocity profiles no longer exhibited distinct patterns associated with individual jets in the downstream region. Turbulence was visually identified by small-scale velocity fluctuations. The turbulent region extended up to approximately $z/D = 12$, above which the crossflow showed no small-scale velocity fluctuations. The blue contours roughly

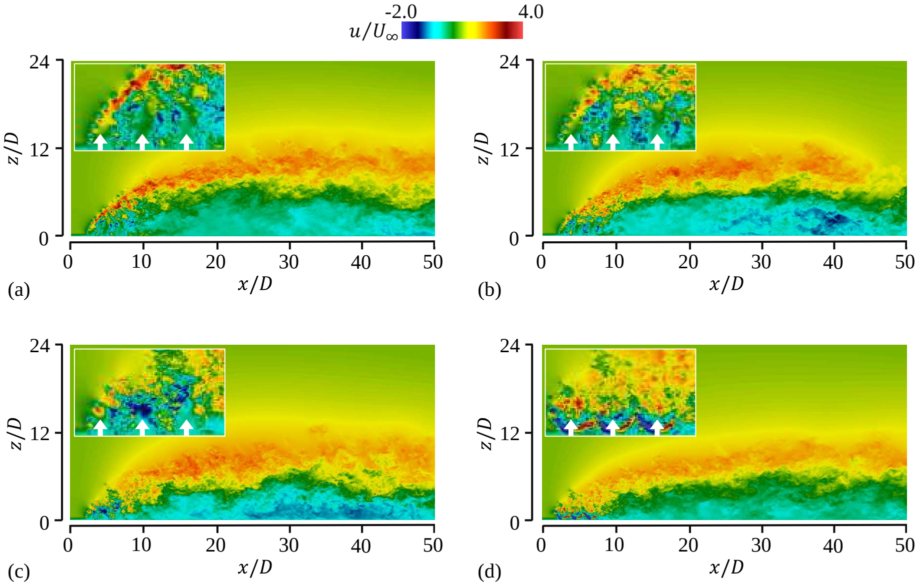

FIG. 4. Streamwise velocity on the xz plane at $y = 5D$, passing through the jet center. Each panel presents the velocity distribution for a different swirl number: (a) $Sw = 0$; (b) $Sw = 0.2$; (c) $Sw = 0.4$; (d) $Sw = 0.6$. Insets show close-up images near the jet array, with arrows indicating the jet locations.

indicate reverse flow regions. It is known that multiple jets can block a crossflow when arranged in the spanwise direction.[19] This blocking effect generates low-pressure regions behind the jets and forms large-scale spanwise vortices, which induce reverse flow near the wall. At this time instant, the reverse flow was particularly prominent for $Sw = 0.2$ and 0.4, as also confirmed below in the mean velocity profiles.

Figure 5 visualizes the temperature T on the same plane and at the same time as Fig. 4. The insets show close-up images of the jet regions. On this plane, three jets with large T values were issued from the bottom around $x/D = 5$. These three jets are clearly visible for $Sw = 0$, 0.2, and 0.4. The potential core of each jet is defined as a region of the jet fluid unmixed with the external fluid, and was identified as the region of constant values of velocity $w/U_J = 1$ or temperature $T/T_0 = 1$. The potential cores, identified by $T/T_0 = 1$, were shortened for stronger swirl cases (i.e., larger Sw). When a jet includes swirl, significant

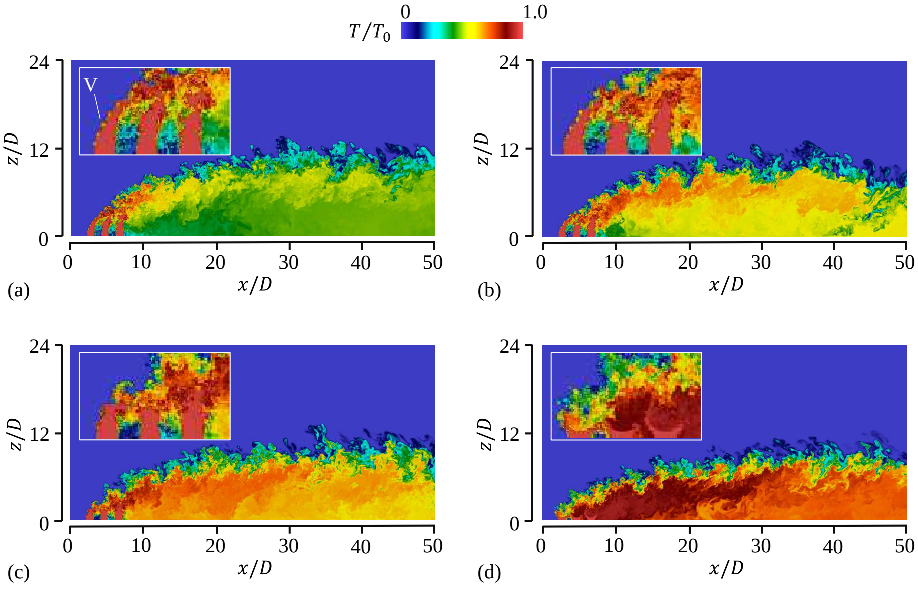

FIG. 5. Temperature on the same xz plane and at the same time as in Fig. 4. Each panel presents the temperature distribution for a different swirl number: (a) $Sw = 0$; (b) $Sw = 0.2$; (c) $Sw = 0.4$; (d) $Sw = 0.6$. Insets show close-up images near the jet array.

fluctuations occur in both the axial and tangential velocity components near the jet exit. As a result, turbulent mixing is enhanced when compared to non-swirling cases, leading to a shorter potential core.[44,45] This feature, observed for a single swirl jet, is consistent with the multiple swirling JICFs considered in the present DNS. Due to the radial velocity induced by very strong swirl, the jet spreads significantly in the radial direction, causing a pressure drop inside the jet and resulting in reverse downward flow.[14] The reverse flow inside the jet, defined by the downward velocity $w < 0$, collapses the jet core. Consequently, for $Sw = 0.6$, the potential cores of the jets immediately disappeared. As Sw increased, the vertical transport due to the jets was inhibited due to the reduction in potential core length. Therefore, turbulent jets at large Sw tend to remain at lower z, and high-temperature fluid from the jets remains near the wall in the downstream region.

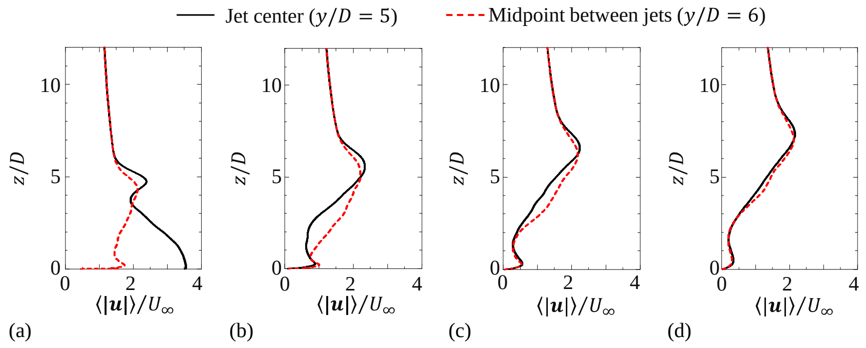

FIG. 6. Vertical profiles of the average of velocity magnitude $\langle|\boldsymbol{u}|\rangle$ at the center of the jet ($y/D = 5$) and between the jets ($y/D = 6$) for $Sw = 0$. Panels show the profiles at different streamwise locations: (a) $x/D = 6.7$, (b) $x/D = 8.6$, (c) $x/D = 10.4$, and (d) $x/D = 12.2$.

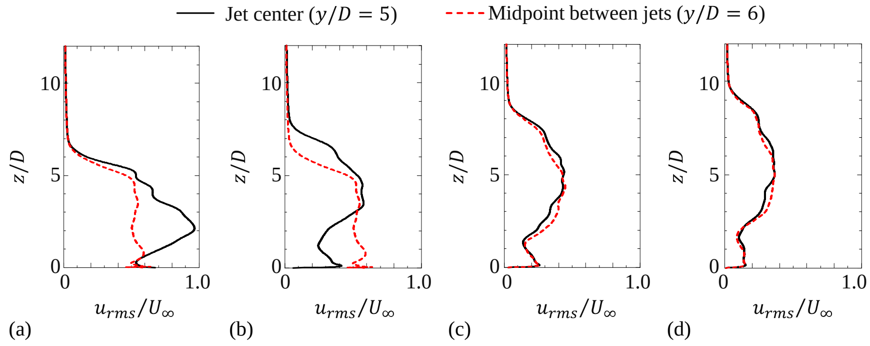

FIG. 7. Vertical profiles of rms streamwise velocity fluctuations u_{rms} at the center of the jet ($y/D = 5$) and between the jets ($y/D = 6$) for $Sw = 0$. Panels show the profiles at different streamwise locations: (a) $x/D = 6.7$, (b) $x/D = 8.6$, (c) $x/D = 10.4$, and (d) $x/D = 12.2$.

B. Velocity and temperature statistics

Figure 6 presents the vertical distributions of the average of velocity magnitude $\langle|\boldsymbol{u}|\rangle$ evaluated at different streamwise positions for $Sw = 0$. The distributions are presented for two y locations passing through the jet center at $y/D = 5$ and at the midpoint between adjacent jets in the spanwise direction at $y/D = 6$. In Fig. 6(a), the streamwise position

$x/D = 6.7$ corresponds to the center of the third jet row, as shown in Fig. 1. At this location, the jet possessed a large vertical velocity, resulting in a very large velocity magnitude at the jet center near $z = 0$, whereas in the inter-jet region, the velocity is roughly half of that value. For $0 \leq z/D \lesssim 3$, the strong vertical jet issued at $x/D = 6.7$ led to a noticeably higher $\langle|\boldsymbol{u}|\rangle$ in this region. On the other hand, a peak at approximately $z/D = 4.5$ occurred in both the jet center and inter-jet locations. This peak corresponds to the axial velocity contribution from inclined jets located upstream at $x/D = 2.7$ and $x/D = 4.7$. Above this peak location, the flow was dominated by the crossflow, and the mean velocity became similar between the two y locations examined. In the downstream direction, the peak location, observed at $z/D \approx 4.5$ in Fig. 6(a), shifted upward due to a rise in the jet height. At $x/D = 6.7$ and 8.6, the distributions differed significantly between the jet center and the inter-jet region; however, this difference became small further downstream, and the mean velocity distribution became more uniform in the spanwise direction, as shown in Figs. 6(c, d).

Figure 7 compares the vertical distributions of the rms fluctuations of the streamwise velocity, u_{rms}. As visually confirmed in Fig. 4, velocity fluctuations within the jet region were large and became smaller at larger z. At $x/D = 6.7$ and 8.6 in Figs. 7(a, b), u_{rms} differs between the jet center and the midpoint between jets; however, this difference becomes negligible further downstream in Figs. 7(c, d).

These results confirm that the flow became statistically homogeneous in the spanwise direction as the jets developed and interacted with each other. A similar formation of homogeneous turbulence has been reported in other studies on jet interactions.[46–50] Although the above results are presented for $Sw = 0$, statistical homogeneity is observed for velocity and temperature statistics in all Sw cases.

Figure 8 presents the vertical profiles of mean streamwise velocity between the jets ($y/D = 8.6$) behind the jet array ($x/D = 8.5$). The mean streamwise velocity near the wall was smaller for swirling jets when compared to the non-swirling case ($Sw = 0$). The mainstream near the wall passed through the inter-jet region with $\langle u\rangle > 0$ before the jets merge. However, swirl caused a more rapid collapse of the jet core and promoted the radial transfer of jet fluid, thereby inhibiting the mainstream pass between two jets. This blocking effect is confirmed by the reduced mean streamwise velocity for $z/D \lesssim 4$ in the swirling jet cases.

Figure 9 presents the streamwise mean velocity distribution on the xz plane passing through the jet center at $y/D = 5$. Regions of negative velocity are enclosed by contour

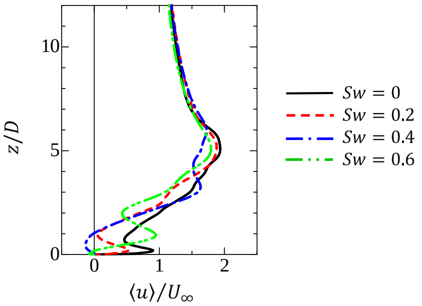

FIG. 8. Vertical profiles of mean streamwise velocity $\langle u \rangle$ between the jets ($y/D = 6$) behind the jet array at $x/D = 8.5$ for different Sw cases.

lines indicating zero velocity (white lines), which separate areas of positive and negative streamwise mean velocity. A reverse flow region with negative streamwise velocity appeared downstream of the jet array. This phenomenon occurred because the spanwise-aligned jet array blocked the mainstream, creating a low-pressure region behind the jets and causing the flow to be drawn toward the wall. In particular, for $Sw = 0.2$ and 0.4, the reverse flow region expanded due to the presence of swirl. This expansion is attributed to the enhanced radial spread of the jets induced by swirl, which intensified the blocking effect by filling the space between the jets with jet fluid, as discussed with Fig. 8. On the other hand, for $Sw = 0.6$, the reverse flow region was smaller than those for moderate swirl cases ($Sw = 0.2$ and 0.4). This reduction was likely due to the collapse of the axial jet flow by the strong swirl motion visualized in Fig. 5(d).

Figure 10 presents the streamwise distribution of the mean streamwise velocity at $y/D = 5.0$ and $z/D = 0.5$. This vertical position z is near the wall and lies within the reverse flow region. Strong reverse flow is observed for $Sw = 0.2$ and 0.4. In particular, for $Sw = 0.2$, the maximum reverse flow velocity was approximately twice that of the non-swirling case ($Sw = 0$). This indicates that adding swirl not only extends the region where reverse flow occurs but also enhances the strength of the reverse flow. For $Sw = 0.2$, the jet-induced blocking effect was strong, resulting in a more pronounced low-pressure region and increased reverse velocity. In contrast, for $Sw = 0.6$, the reverse velocity was small, and the influence of the reverse flow region on the overall flow was limited. The extent of the reverse flow region

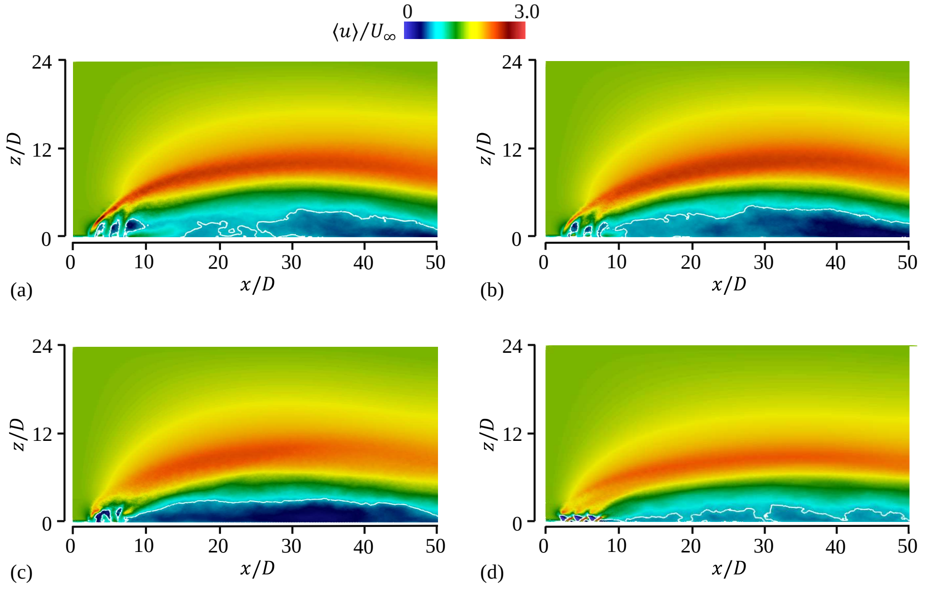

FIG. 9. Mean streamwise velocity distributions on the xz plane at $y/D = 5$. Panels show the velocity distribution for different swirl numbers: (a) $Sw = 0$; (b) $Sw = 0.2$; (c) $Sw = 0.4$; (d) $Sw = 0.6$.

also varied depending on the swirl number. Specifically, the reverse flow region appeared from $x/D = 20$ to $x/D = 50$ for $Sw = 0$ and 0.2, and from the more upstream region for $Sw = 0.4$. This indicates that the influence of reverse flow extends over a broader region in the $Sw = 0.4$ case.

Figure 11 presents the mean temperature distribution on the xz plane. As the swirl strength increased, the entrainment of high-temperature jet fluid toward the wall became more pronounced, resulting in elevated temperatures near the wall. For $Sw = 0.2$ and 0.4, the reverse flow region expanded, and more high-temperature fluid remained near the wall, leading to a more noticeable temperature rise. On the other hand, in the $Sw = 0.6$ case, despite the reverse flow region being smaller, the temperature near the wall remained high. The instantaneous temperature profile near the jets in Fig. 5(d) suggests that this was due to the collapse of the axial flow near the jet exits caused by strong swirl, which suppressed vertical scalar transport and caused high-temperature fluid to accumulate near the wall.

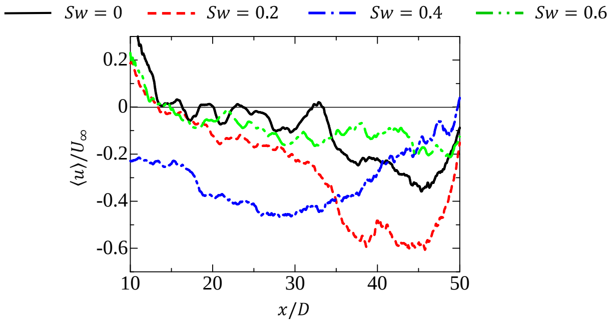

FIG. 10. Streamwise distributions of the mean streamwise velocity at $(y/D, z/D) = (5, 0.5)$, located near the wall.

The swirl number dependence of JICFs was examined using the mean temperature field. The potential core region consists of unmixed jet fluid with $T/T_0 \approx 1$. Accordingly, the potential core height, H_P, is defined as the z-location where the mean temperature $\langle T\rangle/T_0$ decreases to 0.99. Since the jets were inclined in the streamwise direction, H_P was taken as the maximum vertical extent of the isoline $\langle T\rangle/T_0 = 0.99$ on the xz plane intersecting the jet center. This value was evaluated separately for each jet row. Figure 12(a) presents the H_P for each row as a function of Sw. For $Sw = 0$, the potential core height was highest for the first row. Shear layer vortices, marked by "V" in Fig. 5(a), appeared on the upstream side of the first jet. These vortices enhanced three-dimensional turbulence and promoted mixing between the jet and ambient fluid, thereby initiating potential core breakdown. The turbulent jets from the first row then flowed over those in the second and third rows, accelerating their mixing and suppressing their vertical penetration. This jet-to-jet interference explains the reduced H_P for the second and third rows. An increase in Sw results in a decrease in H_P, caused by enhanced mixing between the jet and ambient fluid due to swirl motions.[44] Thus, although rapid core collapse was most prominent at $Sw = 0.6$, even moderate swirl ($Sw = 0.2$ and 0.4) reduced H_P.

The vertical extent of the merged jet, H_J, in the downstream region was also evaluated from the mean temperature profile, defined as the height at which $\langle T\rangle/T_0 = 0.1$. Figure 12(b) plots H_J at $x/D = 10$, 20, and 40 against Sw. In all cases, the jet height increased with x, although the rate of increase became more gradual further downstream due to jet inclination

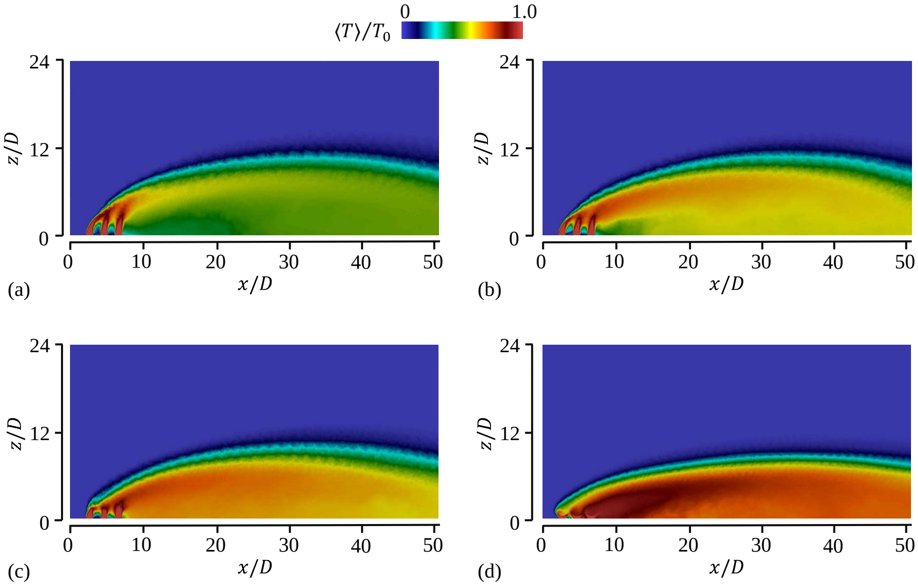

FIG. 11. Mean temperature distributions on the xz plane at $y/D = 5$. Panels show the temperature distributions for different swirl numbers: (a) $Sw = 0$; (b) $Sw = 0.2$; (c) $Sw = 0.4$; (d) $Sw = 0.6$.

by the crossflow. At all streamwise locations, H_J decreased with increasing swirl number.

Figure 12(c) presents the mean wall temperature at $y = 0$, evaluated at the same streamwise locations. For $Sw = 0$ and 0.2, the wall temperature increased with x. In these cases, the jet fluid penetrated the crossflow and did not remain near the wall. In contrast, at $Sw = 0.6$, the wall temperature was already high at $x/D = 10$ due to a rapid collapse of the potential core, as observed in Fig. 5(d). Downstream of this location, the temperature decreased slightly due to vertical diffusion. Overall, increasing swirl promoted confinement of the jet fluid near the wall, resulting in higher mean wall temperatures.

In the vertical distribution of the mean streamwise velocity $\langle u \rangle$ in the fully developed jet region with spanwise homogeneity, $\langle u \rangle$ reached a maximum value inside the jet region and decreased toward U_∞ and 0 in the crossflow and near the wall, respectively. We denote the height at which $\langle u \rangle$ reached its maximum by z_J, and define the jet width δ_J as the distance between two z locations where $\langle u \rangle = 1.5U_\infty$. This threshold was chosen by examining the mean velocity values. Altering the threshold affected the value of δ_J but did not alter the

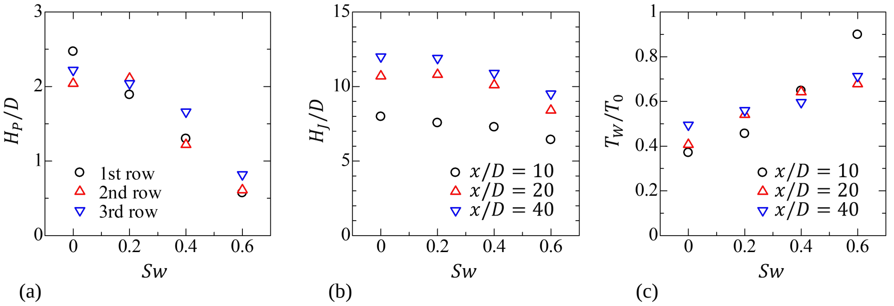

FIG. 12. Swirl number dependence of (a) the potential core height H_P for each jet row, (b) the jet height H_J, and (c) the mean wall temperature T_W. The wall temperature and jet height are evaluated at three streamwise locations.

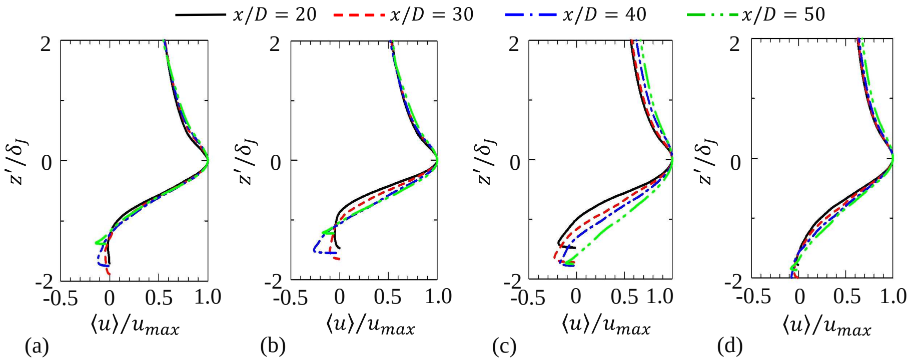

FIG. 13. Vertical profiles of the streamwise mean velocity $\langle u \rangle$ normalized by its maximum value u_{max}, plotted as a function of the distance from the jet center $z' = z - z_J$. The distance is normalized by the jet width δ_J. Panels correspond to different swirl numbers: (a) $Sw = 0$; (b) $Sw = 0.2$; (c) $Sw = 0.4$; (d) $Sw = 0.6$.

main discussion regarding the Sw dependence, as long as the threshold was not too small. Figure 13 presents the mean streamwise velocity $\langle u \rangle$ normalized by its maximum u_{max} as a function of the vertical distance from the jet center $z' = z - z_J$, normalized by the jet width δ_J. This normalization follows previous studies on the self-similar regions of single jets and plumes.[51–55] Figure 13 compares the normalized velocity profiles at different streamwise

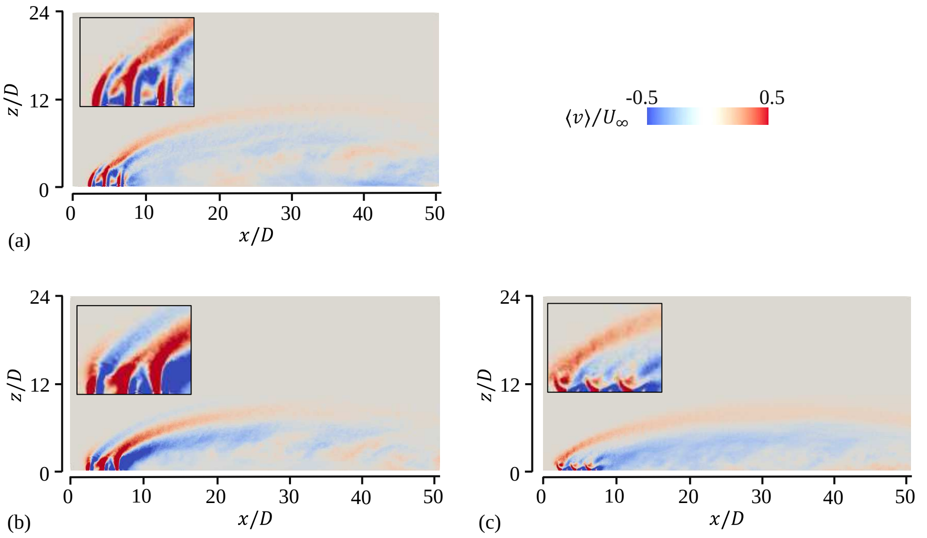

FIG. 14. Mean spanwise velocity distributions on the xz plane at $y/D = 5$. Panels correspond to different swirl numbers: (a) $Sw = 0.2$; (b) $Sw = 0.4$; (c) $Sw = 0.6$. Insets show close-up images near the jet array.

locations for all Sw cases. For $Sw = 0$, the vertical velocity distribution hardly varied with x for $z'/D \geq -1$, and the jet region exhibits self-similarity. This self-similar profile is not observed for swirling jets with $Sw = 0.2$ and 0.4. This difference is attributed to the formation of reverse flow with $\langle u \rangle < 0$ near the wall. Compared with $Sw = 0.2$ and 0.4, $\langle u \rangle$ at $Sw = 0.6$ only weakly depended on x, consistent with the weak reverse flow observed for this case.

For the non-swirling jet case, there was no mean velocity in the spanwise direction. However, the tangential velocity of swirling jets locally generated mean flow in the spanwise direction near the jets. This initial mean flow has the potential to alter the mean flow characteristics in the downstream region. To examine this effect, the mean spanwise velocity $\langle v \rangle$ among different Sw cases was compared. Figure 14 presents the spanwise mean velocity distribution on the xz plane for swirling jets. The interaction of swirling jets with $Sw > 0$ led to the formation of a spanwise mean flow. For $Sw = 0.4$, swirling flows from adjacent jets merged, forming a spanwise mean flow in the downstream region.

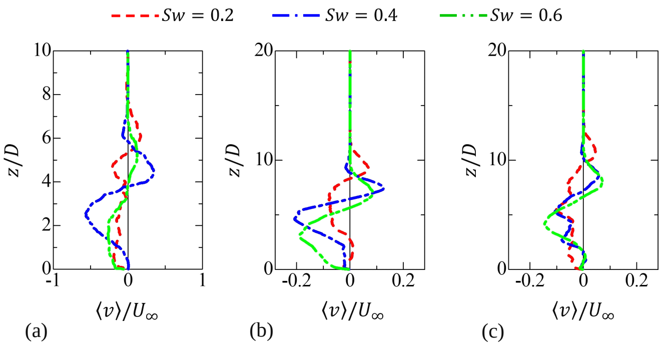

FIG. 15. Vertical distributions of mean spanwise velocity at different streamwise locations: (a) $x/D = 10$, (b) $x/D = 20$, and (c) $x/D = 30$. All results were taken at $y/D = 5$. The range of the vertical axis differed between (a) and (b, c) due to differences in jet height.

Figure 15 presents the vertical distributions of the mean spanwise velocity at $x/D = 10$, 20, and 30. At $x/D = 10$, a strong spanwise mean flow was formed for $Sw = 0.4$, with the mean spanwise velocity reaching approximately half the crossflow velocity. At $x/D = 20$, spanwise mean flows with a similar velocity are observed for both $Sw = 0.4$ and 0.6. For $Sw = 0.4$, the mean velocity was reduced to approximately one-third of its value at $x/D = 10$, whereas for $Sw = 0.6$, the spanwise mean flow was more sustained. The decay of the spanwise mean flow was slower for $Sw = 0.6$, and at $x/D = 30$, the largest spanwise mean velocity is observed for $Sw = 0.6$. In contrast, the decay was faster for $Sw = 0.4$, even though the spanwise mean velocity was initially the largest at $x/D = 10$. Larger Sw resulted in greater tangential velocity in the initial jets. Consequently, the swirl strength affected not only the generation but also the persistence of the spanwise mean flow.

Figure 16 presents the distribution of the rms values for streamwise velocity fluctuations. For $Sw = 0$, the velocity fluctuations in the downstream region were smaller when compared to those for $Sw = 0.2$ and 0.4. In the case of $Sw = 0.2$, large fluctuations are observed near the wall between $x/D = 30$ and 50, while for $Sw = 0.4$, pronounced fluctuations in the jet occurred from $x/D = 20$ to 40. Regions of strong reverse flow coincided with these regions of intense velocity fluctuations, thus indicating a relationship between reverse flow and turbulence generation. It is also evident that adding swirl for $Sw = 0.2$ and 0.4 helped

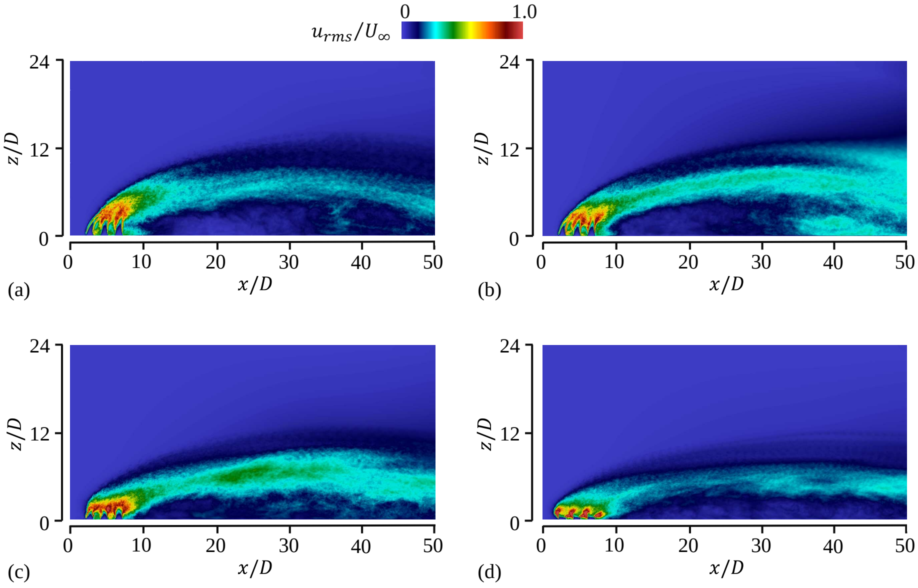

FIG. 16. Distributions of rms streamwise velocity fluctuations u_{rms} on the xz plane at $y/D = 5$. Panels correspond to different swirl numbers: (a) $Sw = 0$; (b) $Sw = 0.2$; (c) $Sw = 0.4$; (d) $Sw = 0.6$.

sustain high turbulence intensity, even in the downstream region. However, for $Sw = 0.6$, the fluctuations were smaller than in the other cases. This reduction was likely due to the collapse of some large structures of the jet, such as the axial flow near the jet exit, resulting in smaller structures with weaker velocity fluctuations, since large structures have dominant contributions to rms velocity fluctuations.

Figure 17 presents the distribution of the rms values for spanwise velocity fluctuations. For $Sw = 0$, spanwise velocity fluctuations were observed near the region where the jet axial flows merge; however, these fluctuations tended to diminish further downstream. In contrast, for $Sw = 0.2$ and 0.4, spanwise velocity fluctuations even remained large in the downstream region. This persistence is attributed to the spanwise mean flow generated by the swirling jets since the vertical gradient of the mean spanwise velocity contributed to the production of spanwise velocity fluctuations, as discussed below. In particular, for $Sw = 0.4$, where strong spanwise mean flow is observed, the spanwise velocity fluctuations were greater

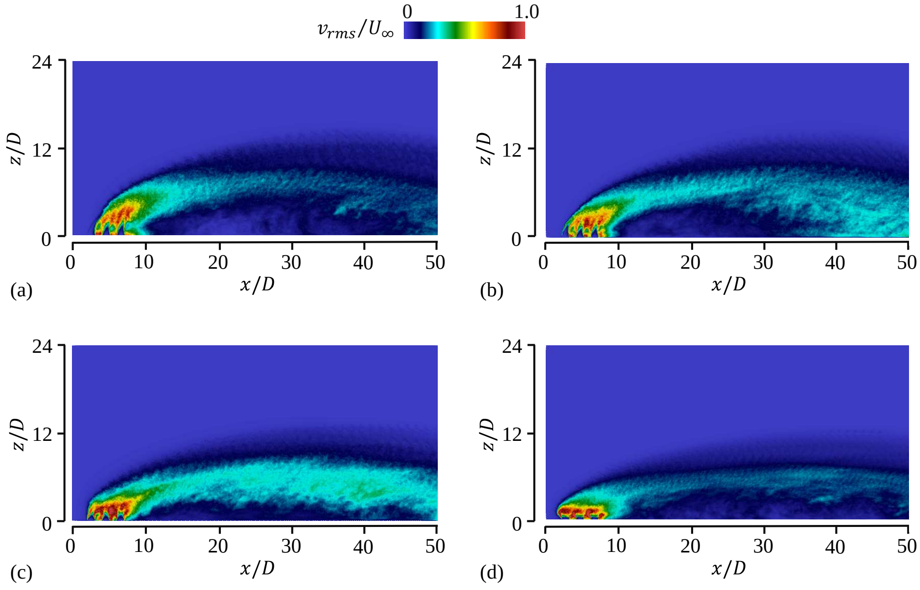

FIG. 17. Same as in Fig. 16, but for rms spanwise velocity fluctuations v_{rms}: (a) $Sw = 0$; (b) $Sw = 0.2$; (c) $Sw = 0.4$; (d) $Sw = 0.6$.

when compared to the other cases. On the other hand, for $Sw = 0.6$, the spanwise velocity fluctuations exhibit a trend similar to that of the streamwise velocity fluctuations.

Figure 18 presents the distribution of the rms values for vertical velocity fluctuations. For $Sw = 0$, 0.2, and 0.4, large vertical velocity fluctuations are observed in the region where the jets merge. In the case of $Sw = 0.6$, significant velocity fluctuations appeared near the jet exit due to the collapse of the axial flow, resulting in highly fluctuating regions at lower vertical positions when compared to the other cases. Furthermore, for $Sw = 0.2$ and 0.4, vertical velocity fluctuations hardly decayed in the downstream region of $x/D \geq 20$, as was also observed for streamwise velocity fluctuations.

Figure 19 presents the distribution of rms values for temperature fluctuations. In all cases, temperature fluctuations were large in the upper part of the jet region. The mean temperature profiles indicate that high-temperature fluid from the swirling jets tends to remain in the near-wall region; however, this region exhibited negligibly small temperature fluctuations. Comparison with the instantaneous temperature profiles shown in Fig. 5 indicates

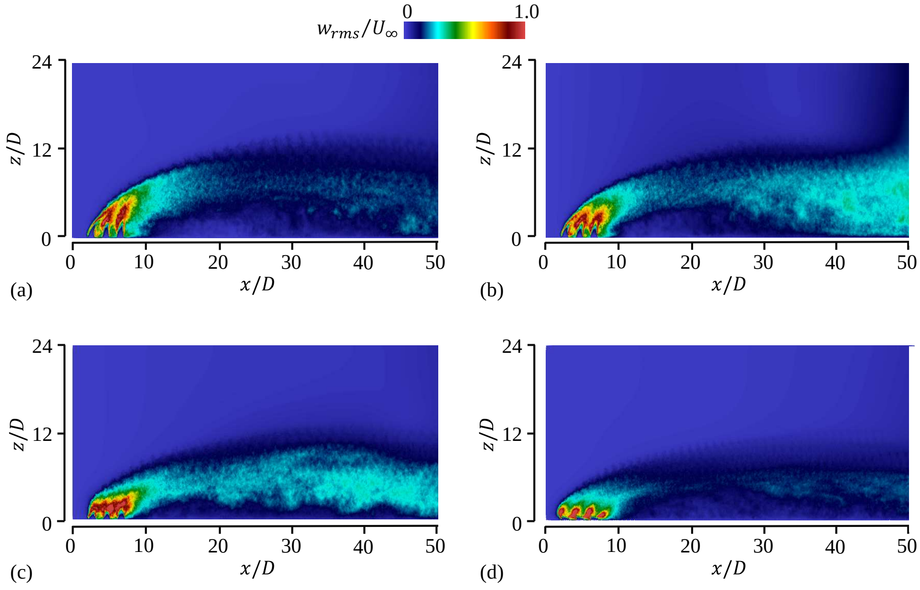

FIG. 18. Same as in Fig. 16, but for rms vertical velocity fluctuations w_{rms}: (a) $Sw = 0$; (b) $Sw = 0.2$; (c) $Sw = 0.4$; (d) $Sw = 0.6$.

that regions of large T_{rms} approximately coincided with the interfacial region between the jets and the crossflow. This region is where mixing occurs between the high-temperature jet fluid and the lower-temperature crossflow, resulting in significant temperature fluctuations. Low rms temperature fluctuations near the wall suggest that the mixing process is limited in this region since the crossflow barely penetrates the jet region.

Figure 20(a) shows the vertical distributions of the vertical flux of temperature fluctuations, $\langle w'T' \rangle$, at $x/D = 12$. Large positive values of $\langle w'T' \rangle$ indicate upward heat transport by turbulent velocity fluctuations. The maximum values of $\langle w'T' \rangle$, denoted by $\langle w'T' \rangle_{max}$, are plotted as a function of Sw in Fig. 20(b). The maximum value decreased with increasing Sw, suggesting that the turbulent merged jets without swirl transported heat more efficiently in the vertical direction.

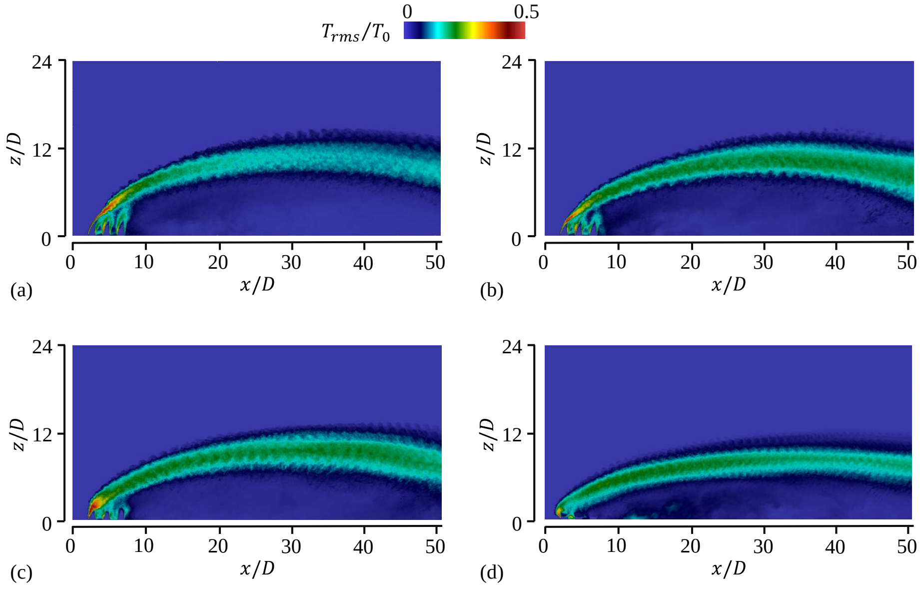

FIG. 19. Distributions of rms temperature fluctuations T_{rms} on the xz plane at $y/D = 5$. Panels correspond to different swirl numbers: (a) $Sw = 0$; (b) $Sw = 0.2$; (c) $Sw = 0.4$; (d) $Sw = 0.6$.

C. Production and dissipation of turbulent kinetic energy

The interaction of swirling jets has been shown to generate a spanwise mean flow with vertical variation, as well as a reverse flow near the wall. The mean shear arising from these flows may serve an important role in the production of turbulent kinetic energy, defined as $k_T = (u_{rms}^2 + v_{rms}^2 + w_{rms}^2)/2$. The turbulence production term is given by the following equation[56]:

$$P = \sum_{\alpha=1}^{3} P_\alpha \quad \text{with} \quad P_\alpha = -\langle u'_\alpha u'_j \rangle \frac{\partial \langle u_\alpha \rangle}{\partial x_j}.$$

The subscript indices $\alpha = 1, 2, 3$ correspond to the x, y, and z directions, respectively. Here, P_α represents the production of the α-directional component of turbulent kinetic energy. Both production and energy dissipation were examined in the flow region where spanwise homogeneity was established, and the statistics were evaluated using time and spanwise averages.

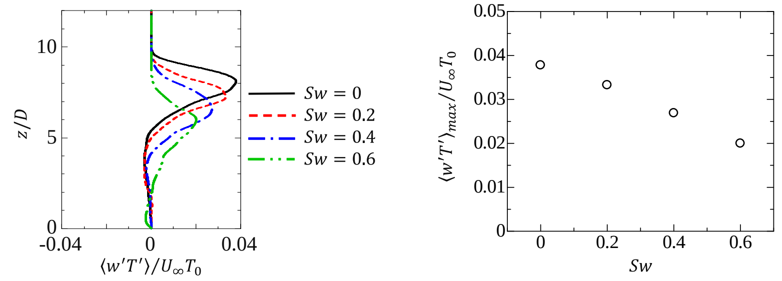

(a) (b)

FIG. 20. (a) Vertical profiles of the vertical turbulent heat flux, $\langle w'T' \rangle$, at $x/D = 12$ for different swirl numbers. (b) Swirl number dependence of the maximum value of $\langle w'T' \rangle$ at $x/D = 12$.

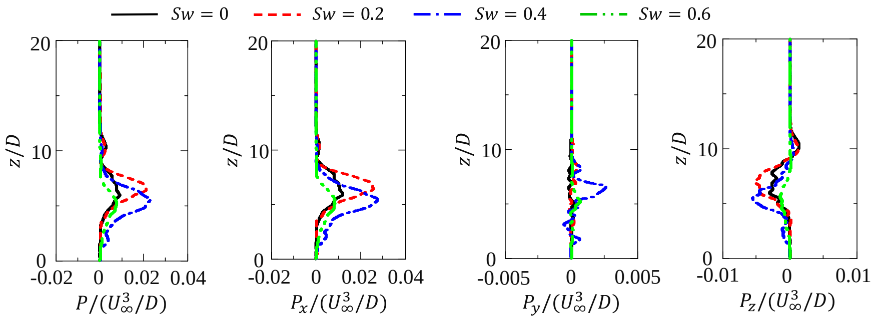

(a) (b) (c) (d)

FIG. 21. Vertical profiles of the production terms of turbulent kinetic energy at $x/D = 20$. Panels show: (a) total production P, (b) streamwise component P_x, (c) vertical component P_y, and (d) spanwise component P_z.

Figures 21 and 22 present the vertical distributions of P, P_x, P_y, and P_z at $x/D = 20$ and 40, respectively. Each figure compares the results for different Sw cases. At $x/D = 20$, the turbulence production P for $Sw = 0.2$ and 0.4 was more than twice that for $Sw = 0$, as shown in Fig. 21(a). Similarly, at $x/D = 40$ in Fig. 22(a), P remained high for $Sw = 0.2$ and 0.4, indicating that swirl enhanced turbulence generation. These results are consistent with the large rms velocity fluctuations in the downstream region for $Sw = 0.2$ and 0.4, as previously discussed in Sec. III B.

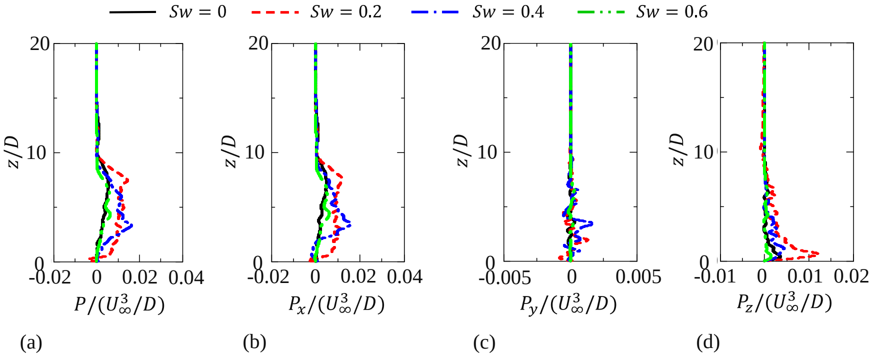

FIG. 22. Vertical profiles of the production terms of turbulent kinetic energy at $x/D = 40$. Panels show: (a) total production P, (b) streamwise component P_x, (c) vertical component P_y, and (d) spanwise component P_z.

For the streamwise component P_x, shown in Figs. 21(b) and 22(b), the profiles closely resemble those of P at both streamwise positions. Here, examination of the three components in P_x suggests that P_x is primarily associated with the vertical gradient of the streamwise mean velocity, $\partial\langle u\rangle/\partial z$, which became pronounced due to the jet inclination by the crossflow. At both streamwise locations, P_x was particularly large for $Sw = 0.2$ and 0.4, which can be attributed to strong vertical gradients in the streamwise mean velocity caused by reverse flow in these cases.

The spanwise component P_y, shown in Figs. 21(c) and 22(c), did not contribute to turbulence production for the non-swirling jets ($Sw = 0$) because the spanwise mean velocity was negligible. However, for swirling jets, which generated a spanwise mean flow, the production of spanwise velocity fluctuations occurred. At $x/D = 20$, large P_y was observed for $Sw = 0.4$, which can be attributed to the vertical gradient of the spanwise mean velocity, as seen in Fig. 15(b). As the spanwise mean flow decayed, P_y for $Sw = 0.4$ also decreased from $x/D = 20$ to 40. Nevertheless, P_y remained about one-tenth of the total production, indicating that the contribution of the spanwise mean flow to overall turbulence production was small. Although the spanwise mean velocity at $x/D = 20$ is similar for $Sw = 0.4$ and 0.6, turbulence production was significantly larger for $Sw = 0.4$ due to small Reynolds stresses in the $Sw = 0.6$ case.

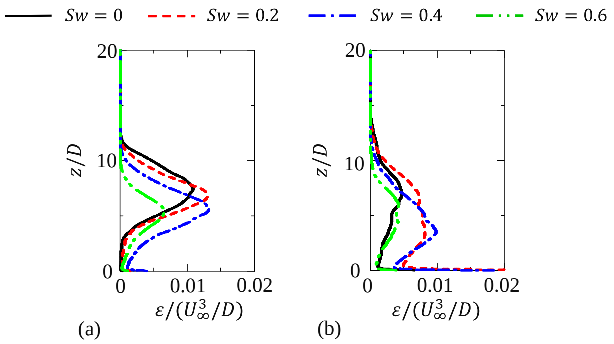

FIG. 23. Vertical profiles of the dissipation rate of turbulent kinetic energy ε. Panels show the profiles at different streamwise locations: (a) $x/D = 20$; (b) $x/D = 40$.

The vertical component P_z tended to be negative at $x/D = 20$, as shown in Fig. 21(d). The streamwise gradient of the mean vertical velocity, $\partial\langle w\rangle/\partial x$, became negative because the vertical flow from the jets weakened as the jets were inclined downstream by the crossflow. This gradient was amplified in the $Sw = 0.2$ and 0.4 cases due to the suppression of the vertical flow of jets. The corresponding Reynolds stress term in P_z, $\langle u'w'\rangle$, is negative on the downstream side of the jets due to the mean shear effect of $\partial\langle u\rangle/\partial z > 0$, which is consistent with a well-known behavior for turbulent shear flows.[57] Thus, the inclination of the jets led to negative P_z due to $\langle u'w'\rangle(\partial\langle w\rangle/\partial x) > 0$, which was more significant in swirling jet cases due to the suppression of vertical flow. This behavior reflects the counter-gradient transport of vertical momentum in the crossflow direction. At $x/D = 20$, P_z accounted for approximately 25% of total turbulence production for $Sw = 0.2$ and 0.4, thus highlighting its importance in the overall turbulent kinetic energy budget. At $x/D = 40$, the negative production became negligible, as seen in Fig. 22(d). However, P_z became positive and large near the wall for $Sw = 0.4$, indicating active turbulence production. This is attributed to the formation of a low-pressure region near the wall that induced strong downward flow, leading to positive P_z in that region. This positive production term at $Sw = 0.4$ explains the enhanced vertical velocity fluctuations in the downstream region observed in Fig. 18(c).

The dissipation rate of turbulent kinetic energy is defined as

$$\varepsilon = \nu \left\langle \left(\frac{\partial u_i'}{\partial x_j} \right)^2 \right\rangle .$$

The scaling of energy dissipation is crucial in turbulence theories and modeling.[58] Figure 23 presents the vertical distributions of ε at $x/D = 20$ and 40. At $x/D = 20$, the ε values for $Sw = 0, 0.2$, and, 0.4 are comparable, while the $Sw = 0.6$ case exhibits noticeably smaller values. At $x/D = 40$, the difference in ε of the $Sw = 0.2$ and 0.4 cases from the others became more pronounced. In turbulent shear flows, the dissipation rate approximately balances the production term.[59–61] The large dissipation rate for $Sw = 0.2$ and 0.4 is attributed to enhanced turbulence production due to swirl, which sustains strong velocity fluctuations further downstream. At all streamwise positions, ε was smallest for $Sw = 0.6$ due to reduced velocity fluctuations caused by the collapse of the axial flow in the jets.

Turbulence theories and models often describe dissipation rates using a non-dimensional parameter called the dissipation coefficient or non-dimensional dissipation rate, C_ε, which is defined as

$$\varepsilon = C_\varepsilon \frac{\mathcal{U}^2}{\mathcal{T}},$$

where $\mathcal{U}$ and $\mathcal{T}$ are the characteristic velocity and time scales of large-scale motions, respectively.[56] The time scale is often estimated as the ratio between the integral scale (defined by the velocity auto-correlation function) and the rms velocity fluctuations. When turbulence with small fluctuations is advected by a mean flow, the integral scale is frequently estimated from the integral time scale using Taylor's frozen turbulence hypothesis. However, this approach is not suitable for JICFs due to the high turbulence intensity, as indicated by the large u_{rms}/U_∞, v_{rms}/U_∞, and w_{rms}/U_∞ values. For this reason, the present study evaluated the spanwise integral length scale L_w, defined via the longitudinal auto-correlation function of the spanwise velocity:

$$R_z(r_z; x, y) = \frac{\langle w'(x, y, z, t)\, w'(x, y, z + r_z, t)\rangle}{w_{rms}^2(x, y)},$$

and

$$L_w = \int_0^{r_{z0}} R_z \, dz,$$

where r_{z0} is the first zero-crossing point of R_z. The present study considered the integral scale in the spanwise direction, where the flow is statistically homogeneous, because the streamwise and vertical integral scales involve velocity correlations between statistically non-equivalent points, making their interpretation challenging. The dissipation coefficient was then evaluated as $C_\varepsilon = \varepsilon/(\mathcal{U}^2/\mathcal{T})$, with $\mathcal{U} = \sqrt{2k_T}$ and $\mathcal{T} = L_w/w_{rms}$, in the fully developed jet region exhibiting spanwise homogeneity ($x/D \geq 15$) at the height corresponding to the maximum value of the dissipation rate. Different estimations were also tested for the velocity scale $\mathcal{U}$, such as rms velocity fluctuations in each direction. Comparisons of C_ε confirmed that this change did not affect the discussion given below.

Figure 24 shows the streamwise variation of the integral scale L_w. As the jets evolved downstream, L_w gradually increased. For swirling jets with $Sw = 0.4$, L_w was approximately twice as large as in the other cases. It is known that mean shear promotes the growth of the turbulence length scale in the shear direction.[62] In the present flow setup, the vertical gradient of the spanwise mean velocity $\partial\langle v\rangle/\partial z$ enhanced the spanwise integral scale. A strong spanwise mean flow due to swirl jet interaction was observed upstream of $x/D = 10$ for $Sw = 0.4$, as shown in Fig. 15. Turbulence in the jet region at $Sw = 0.4$ experienced mean shear from this upstream spanwise flow, resulting in larger L_w.

Figure 25(a) presents the streamwise variations of the turbulent Reynolds number $Re_\lambda = (2k_T/3)\sqrt{15/\nu\varepsilon}$ and the non-dimensional dissipation C_ε. The turbulent Reynolds number increased in the streamwise direction. Since the jet array was periodically arranged in the spanwise direction, the merged jet became statistically homogeneous in that direction. Similarly, planar jets, with spanwise homogeneity, are known to exhibit increasing Re_λ in the jet flow direction. In contrast, C_ε decreased with x for $x/D \lesssim 30$ and then asymptotically approached a constant value of approximately $C_\varepsilon \approx 0.4$. These trends are further visualized in the $(Re_\lambda, C_\varepsilon)$ plot in Fig. 25(b). In high-Reynolds-number turbulence, C_ε became independent of Re_λ under equilibrium conditions between the energy cascade and dissipation. However, in non-equilibrium conditions, a scaling $C_\varepsilon \sim Re_\lambda^{-1}$ is often observed in various canonical flows.[58] The present DNS data also followed the $C_\varepsilon \sim Re_\lambda^{-1}$ trend, as shown by the dashed line in Fig. 25(b). This inverse scaling held in the upstream region ($x/D \lesssim 30$), while C_ε stabilized around 0.4 in the downstream region. The transition from the non-equilibrium to equilibrium state was consistently observed regardless of Sw, and appeared to be independent of the swirl effects observed in other velocity and temperature statistics. Similar asymptotic values of C_ε, typically ranging between 0.4 and 0.6, have been reported in other turbulent flows, including turbulent mixing layers and grid-generated turbulence.[63–65] However, these values should not be regarded as universal; even for grid turbulence, significant variations in C_ε have been reported depending on experimental conditions and the choice of characteristic scales. The present results suggest that turbulence generated by multiple

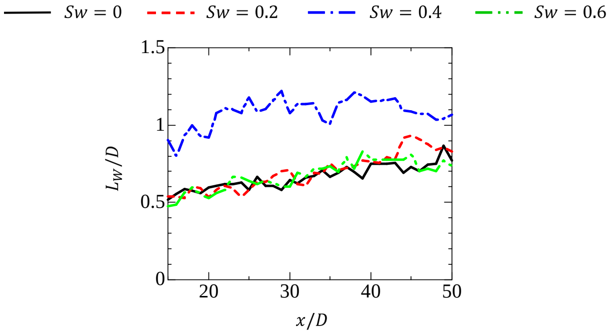

FIG. 24. Streamwise variations of the integral scale L in the fully developed jet region with spanwise homogeneity ($x/D \geq 15$) at the vertical locations where the maximum dissipation rate reaches the peak.

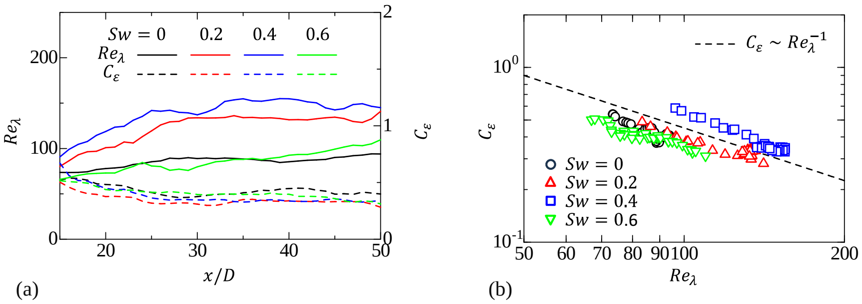

FIG. 25. (a) Streamwise variations of the turbulent Reynolds number Re_λ and the non-dimensional dissipation rate C_ε in the fully developed jet region with spanwise homogeneity ($x/D \geq 15$) at the vertical locations where the maximum dissipation rate reaches the peak. (b) Variations of C_ε as a function of Re_λ.

JICFs exhibits similar C_ε values to those observed in other canonical turbulent flows; however, to the best of our knowledge, existing studies on JICF have not explicitly quantified C_ε.

IV. CONCLUSION

The present study has reported the DNS results of multiple slightly heated swirling JICFs. The effects of swirl were investigated by comparing cases with swirl numbers Sw ranging from 0 to 0.6 while keeping the jet Reynolds number and the jet–crossflow velocity ratio fixed at 2100 and 3.3, respectively. A total of 15 jets were arranged in three rows along the streamwise direction and five columns in the spanwise direction, with periodicity assumed in the spanwise direction. Notably, swirl motion shortened the jet potential core. Moderate swirl ($Sw = 0.2$–0.4) reduced jet height and induced strong reverse flow near the wall. Due to this enhanced reverse flow, the mean velocity profile did not exhibit self-similarity, which was observed in the non-swirl case. In the strong swirl case ($Sw = 0.6$), the potential core collapsed immediately after the jet exited, resulting in jet penetration into the crossflow being significantly suppressed. These swirl effects caused high-temperature fluid from the jets to remain near the wall in the downstream region. For moderate swirl, the interaction of multiple swirling jets generated a spanwise mean flow after the jets merged. The resulting vertical shear increased the spanwise integral scale; however, turbulence production due to this spanwise shear contributed only approximately 10% of the total. In contrast, modifications to the streamwise mean velocity, such as the formation of reverse flow, substantially enhanced turbulence production, leading to strong velocity fluctuations that persisted downstream. An analysis of the energy dissipation rate indicates that the non-dimensional dissipation rate C_ε scales inversely with the turbulent Reynolds number after the jet interaction, indicating the presence of non-equilibrium turbulence, where the energy cascade and dissipation are imbalanced. Further downstream, C_ε approached a constant value, signifying a transition to equilibrium turbulence. Although the Reynolds number in the present DNSs is moderate and lower than those in industrial applications, the DNSs presented here highlights the significant role of swirl in modifying jet interaction, turbulence, and scalar transport in JICF configurations, offering novel insights into similar flows encountered in industrial applications such as air-cooled heat exchangers.

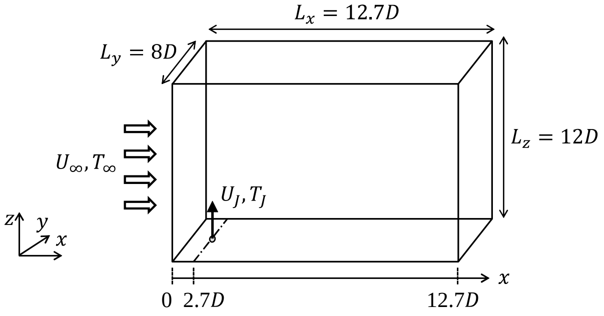

FIG. 26. Schematic of the DNS of a single jet issued into a crossflow.

ACKNOWLEDGMENTS

The authors acknowledge Prof. R. Onishi (Institute of Science Tokyo), Dr. S. Qian (JGC Corporation), and Mr. X. Hu (JGC Corporation) for their fruitful discussions. This work was supported by JSPS KAKENHI Grant Nos. JP23K22669 and JP25K01155. DNSs were performed using high-performance computing systems at the Japan Agency for Marine-Earth Science and Technology and Nagoya University. This work was supported by the Collaborative Research Project on Computer Science with High-Performance Computing at Nagoya University.

DATA AVAILABILITY

The data supporting the findings of this study are available from the corresponding author upon reasonable request.

Appendix A: DNS of a single jet issued into a crossflow

An additional DNS was conducted for a single jet issued into a crossflow to validate the present numerical methods. Figure 26 presents a schematic of the flow setup. The jet was issued from a hole located at $x/D = 2.7$ from the inlet of the crossflow. The domain size was $(L_x, L_y, L_z) = (12.7D, 8D, 12D)$, discretized using regular grids with $(N_x, N_y, N_z) = (1016, 640, 960)$ grid points. Uniform grids were used in the y direction, while the grid spacing

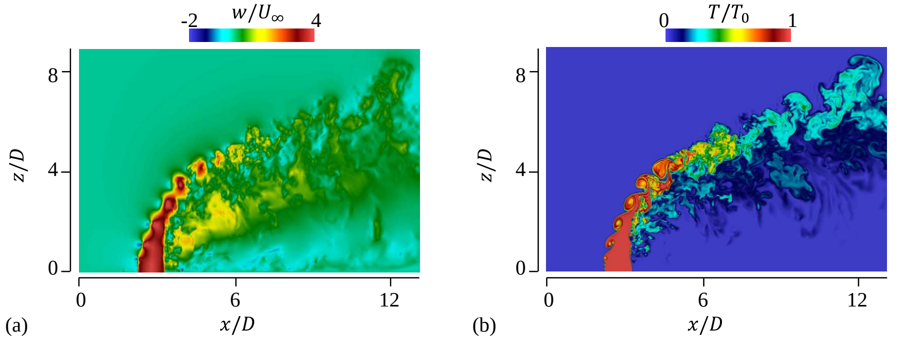

FIG. 27. Visualizations of (a) vertical velocity and (b) temperature on the center plane of the jet.

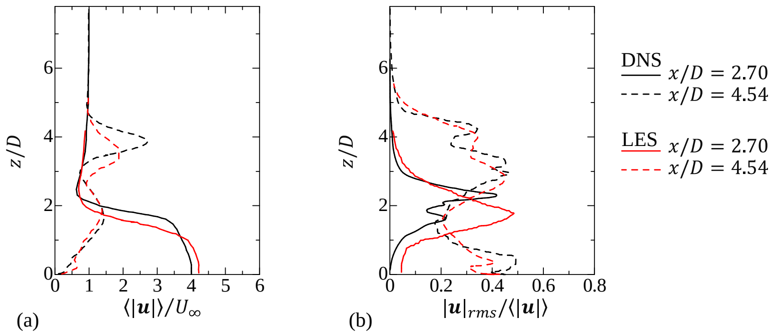

FIG. 28. Vertical profiles of (a) mean and (b) rms fluctuations of velocity magnitude at $x/D = 2.70$ and 4.54. These results are compared with LES data.[22]

in the x and z directions was refined near the jet exit. The grid points were specified using a hyperbolic tangent function, with the same formulation as in Sec. II and Ref. 66. The DNS code was identical to that used for the multiple jet cases. Boundary conditions were also the same, except in the y direction, where slip boundary conditions were applied. The simulation was performed at a jet Reynolds number of $Re_J = U_J D/\nu = 2100$, a Prandtl number of $Pr = \nu/\alpha = 1$, and a velocity ratio of $U_J/U_\infty = 3.3$, consistent with the multiple jet cases. These U_J/U_∞ and Re_J values are the same as those used in the LES by Yuan et al.[22], with which the present DNS is compared. Flow statistics were evaluated after $t = 100(D/U_\infty)$, by which time the flow reached a statistically steady state.

Figure 27 visualizes the vertical velocity w and temperature deviation T on the xz plane crossing the jet center. The jet was inclined by the crossflow, and the high-temperature fluid was advected downstream. Velocity fluctuations were also induced in the wake behind the jet, even near the wall, due to the presence of wake vortices, as observed in a previous JICF study.[2]

Figure 28 presents vertical profiles of the mean and rms fluctuations of velocity magnitude $|\boldsymbol{u}|$, denoted by $\langle|\boldsymbol{u}|\rangle$, and $|\boldsymbol{u}|_{rms} = \sqrt{\langle|\boldsymbol{u}|^2\rangle - \langle|\boldsymbol{u}|\rangle^2}$, at $x/D = 2.70$ and 4.54. The present results are compared with LES data from Ref. 22. The location $x/D = 2.70$ corresponds to the center of the jet exit, where the mean velocity magnitude is largest near $z = 0$. The velocity at this location decreases with x due to the collapse of the potential core and the jet's inclination caused by the crossflow. At $x/D = 4.54$, the mean velocity reaches its maximum at $z/D \approx 4$, corresponding to the height of the jet observed in Fig. 27, and a secondary peak appears around $z/D \approx 2$. The rms velocity fluctuations at $x/D = 2.70$ became large near $z/D \approx 2$, where the vertical gradient of the mean velocity was large. Notably, large fluctuations were associated with vortices generated by shear instability at the jet edge, as seen in the temperature profile on the upstream side of the jet potential core in Fig. 27(b). At $x/D = 4.54$, fluctuations were pronounced around $z/D \approx 3$ and 0.5, reflecting jet fluctuations and wake vortices near the wall, respectively.

These distributions are qualitatively consistent with previous LES results, indicating that the present DNS captured the key features of JICFs. However, differences in profile details were observed. Shear instability in jets is sensitive to disturbances both inside and outside the jet, and jet evolution—including mean velocity and Reynolds stress profiles—often varies among experiments and numerical simulations.[51,67–70] A related issue has also been investigated for a jet issued into a turbulent crossflow.[71] This sensitivity leads to variations in velocity statistics, as also reflected in the differences between the present DNS and LES results.

REFERENCES

[1] A. R. Karagozian, "The jet in crossflow," Phys. Fluids **26**, 101303 (2014).

[2] T. F. Fric and A. Roshko, "Vortical structure in the wake of a transverse jet," J. Fluid Mech. **279**, 1 (1994).

[3]S. H. Smith and M. G. Mungal, "Mixing, structure and scaling of the jet in crossflow," J. Fluid Mech. **357**, 83 (1998).

[4]Y. Kamotani and I. Greber, "Experiments on a turbulent jet in a cross flow," AIAA J. **10**, 1425 (1972).

[5]J. Andreopoulos, "On the structure of jets in a crossflow," J. Fluid Mech. **157**, 163 (1985).

[6]K. Mahesh, "The interaction of jets with crossflow," Annu. Rev. Fluid Mech. **45**, 379 (2013).

[7]R. I. Sykes, W. S. Lewellen, and S. F. Parker, "On the vorticity dynamics of a turbulent jet in a crossflow," J. Fluid Mech. **168**, 393 (1986).

[8]S. L. V. Coelho and J. C. R. Hunt, "The dynamics of the near field of strong jets in crossflows," J. Fluid Mech. **200**, 95 (1989).

[9]X. Hu, R. Onishi, and S. Qian, "Wake vortex formation and its role in turbulent heat transport in jet in crossflow," Phys. Fluids **36**, 095167 (2024).

[10]R. J. Berryman and C. M. B. Russell, "Airflow in air-cooled heat exchangers," Heat Transfer Eng. **8**, 40 (1987).

[11]M. F. M. Fahmy and H. I. Nabih, "Impact of ambient air temperature and heat load variation on the performance of air-cooled heat exchangers in propane cycles in LNG plants–Analytical approach," Energy Convers. Manage. **121**, 22 (2016).

[12]S. Ghani, S. M. A. Gamaledin, F. Bakochristou, E. El-Bialy, M. M. Mohamed, and R. M. E. H. Elsawi, "Numerical and wind tunnel investigation of hot air recirculation across liquefied natural gas air cooled heat exchangers," J. Wind Eng. Ind. Aerodyn. **172**, 409 (2018).

[13]W. Deng, F. Sun, K. Chen, and X. Zhang, "New method to decrease the air recirculation of mechanical draft wet cooling tower group by increasing height of fan duct," Appl. Therm. Eng. **219**, 119645 (2023).

[14]J. A. Denev, J. Fröhlich, and H. Bockhorn, "Large eddy simulation of a swirling transverse jet into a crossflow with investigation of scalar transport," Phys. Fluids **21**, 015101 (2009).

[15]D. Yu, M. S. Ali, and J. H. W. Lee, "Multiple tandem jets in cross-flow," J. Hydr. Eng. **132**, 971 (2006).

[16]Z. Li, W. Huai, and Z. Qian, "Study on the flow field and concentration characteristics of the multiple tandem jets in crossflow," Sci. China Technol. Sci. **55**, 2778 (2012).

[17]S. Maikap and A. K. Rajagopal, "Flow physics of supersonic crossflow with transversely

injected jets in streamwise tandem configuration," Phys. Fluids **37**, 036113 (2025).

[18] B. Zang and T. H. New, "Near-field dynamics of parallel twin jets in cross-flow," Phys. Fluids **29**, 035103 (2017).

[19] I. Franco, A. Gutiérrez, and J. Cataldo, "Row of jets in cross-flow as wind barrier," J. Wind Eng. Indust. Aerodyn. **223**, 104937 (2022).

[20] S. Maikap, "Investigation of mixing characteristics and flow physics induced by spanwise tandem injection in supersonic crossflow," Phy. Rev. Fluids **9**, 093401 (2024).

[21] P. J. Kristo and M. L. Kimber, "Cylinders and jets in crossflow: Wake formations as a result of varying geometric proximities," Phys. Fluids **33**, 055106 (2021).

[22] L. L. Yuan, R. L. Street, and J. H. Ferziger, "Large-eddy simulations of a round jet in crossflow," J. Fluid Mech. **379**, 71 (1999).

[23] Y. Dai, T. Kobayashi, and N. Taniguchi, "Large eddy simulation of plane turbulent jet flow using a new outflow velocity boundary condition," JSME Int. J., Ser. B **37**, 242 (1994).

[24] Z. Gu, H. Li, W. Zhang, Y. Li, and J. Peng, "Wind tunnel simulation on re-circulation of air-cooled condensers of a power plant," J. Wind Eng. Indust. Aerodyn. **93**, 509 (2005).

[25] Z. Gu, X. Chen, W. Lubitz, Y. Li, and W. Luo, "Wind tunnel simulation of exhaust recirculation in an air-cooling system at a large power plant," Int. J. Therm. Sci. **46**, 308 (2007).

[26] P. Liu, H. Duan, and W. Zhao, "Numerical investigation of hot air recirculation of air-cooled condensers at a large power plant," Appl. Therm. Eng. **29**, 1927 (2009).

[27] H. Fellouah, C. G. Ball, and A. Pollard, "Reynolds number effects within the development region of a turbulent round free jet," Int. J. Heat Mass Transfer **52**, 3943 (2009).

[28] G. P. Romano, "Large and small scales in a turbulent orifice round jet: Reynolds number effects and departures from isotropy," Int. J. Heat Fluid Flow **83**, 108571 (2020).

[29] M. Takahashi, R. Fukui, K. Tsujimoto, T. Ando, and T. Shakouchi, "Helical structures in a temporally developing round jet in the developed state," Flow, Turbul. Combust. **111**, 59 (2023).

[30] S. J. Kwon and I. W. Seo, "Reynolds number effects on the behavior of a non-buoyant round jet," Exp. Fluids **38**, 801 (2005).

[31] Y. Morinishi, T. S. Lund, O. V. Vasilyev, and P. Moin, "Fully conservative higher order finite difference schemes for incompressible flow," J. Comput. Phys. **143**, 90 (1998).

[32] T. Katagiri, T. Watanabe, and K. Nagata, "Statistical properties of a model of a turbulent

patch arising from a breaking internal wave," Phys. Fluids **33**, 055107 (2021).

[33]M. Hayashi, T. Watanabe, and K. Nagata, "The relation between shearing motions and the turbulent/non-turbulent interface in a turbulent planar jet," Phys. Fluids **33**, 055126 (2021).

[34]M. Hayashi, T. Watanabe, and K. Nagata, "Characteristics of small-scale shear layers in a temporally evolving turbulent planar jet," J. Fluid Mech. **920**, A38 (2021).

[35]T. Watanabe, Y. Sakai, K. Nagata, Y. Ito, and T. Hayase, "Turbulent mixing of passive scalar near turbulent and non-turbulent interface in mixing layers," Phys. Fluids **27**, 085109 (2015).

[36]T. Watanabe, J. J. Riley, and K. Nagata, "Effects of stable stratification on turbulent/nonturbulent interfaces in turbulent mixing layers," Phys. Rev. Fluids **1**, 044301 (2016).

[37]T. Watanabe, J. J. Riley, K. Nagata, K. Matsuda, and R. Onishi, "Hairpin vortices and highly elongated flow structures in a stably stratified shear layer," J. Fluid Mech. **878**, 37 (2019).

[38]T. Watanabe, X. Zhang, and K. Nagata, "Turbulent/non-turbulent interfaces detected in DNS of incompressible turbulent boundary layers," Phys. Fluids **30**, 035102 (2018).

[39]X. Zhang, T. Watanabe, and K. Nagata, "Reynolds number dependence of the turbulent/non-turbulent interface in temporally developing turbulent boundary layers," J. Fluid Mech. **964**, A8 (2023).

[40]T. Watanabe and K. Nagata, "Integral invariants and decay of temporally developing grid turbulence," Phys. Fluids **30**, 105111 (2018).

[41]T. Watanabe, Y. Zheng, and K. Nagata, "The decay of stably stratified grid turbulence in a viscosity-affected stratified flow regime," J. Fluid Mech. **946**, A29 (2022).

[42]X. Zhang, T. Watanabe, and K. Nagata, "Turbulent/nonturbulent interfaces in high-resolution direct numerical simulation of temporally evolving compressible turbulent boundary layers," Phys. Rev. Fluids **3**, 094605 (2018).

[43]X. Zhang, T. Watanabe, and K. Nagata, "Passive scalar mixing near turbulent/non-turbulent interface in compressible turbulent boundary layers," Phys. Scr. **94**, 044002 (2019).

[44]J. Panda and D. K. McLaughlin, "Experiments on the instabilities of a swirling jet," Phys. Fluids **6**, 263 (1994).

[45] R. Örlü and P. H. Alfredsson, "An experimental study of the near-field mixing characteristics of a swirling jet," Flow, Turbul. and Combust. **80**, 323 (2008).

[46] S. Ghahremanian, K. Svensson, M. J. Tummers, and B. Moshfegh, "Near-field mixing of jets issuing from an array of round nozzles," Int. J. Heat Fluid Flow **47**, 84 (2014).

[47] S. Tan, X. Xu, Y. Qi, and R. Ni, "Scalings and decay of homogeneous, nearly isotropic turbulence behind a jet array," Phys. Rev. Fluids **8**, 024603 (2023).

[48] T. Mori, T. Watanabe, and K. Nagata, "Nearly homogeneous and isotropic turbulence generated by the interaction of supersonic jets," Exp. Fluids **65**, 47 (2024).

[49] T. Watanabe, T. Mori, K. Ishizawa, and K. Nagata, "Scale dependence of local shearing motion in decaying turbulence generated by multiple-jet interaction," J. Fluid Mech. **997**, A14 (2024).

[50] T. Watanabe, T. Inagaki, T. Mori, K. Ishizawa, and K. Nagata, "Direct numerical simulations of the interaction of temporally evolving circular jets," J. Fluid Mech. **1009**, A68 (2025).

[51] R. C. Deo, J. Mi, and G. J. Nathan, "The influence of Reynolds number on a plane jet," Phys. Fluids **20**, 075108 (2008).

[52] T. Watanabe, Y. Sakai, K. Nagata, O. Terashima, and T. Kubo, "Simultaneous measurements of reactive scalar and velocity in a planar liquid jet with a second-order chemical reaction," Exp. Fluids **53**, 1369 (2012).

[53] O. Terashima, Y. Sakai, Y. Goto, K. Onishi, K. Nagata, and Y. Ito, "On the turbulent energy transport related to the coherent structures in a planar jet," Exp. Therm. Fluid Sci. **68**, 697 (2015).

[54] M. Takahashi, K. Iwano, Y. Sakai, and Y. Ito, "Experimental investigation on destruction of Reynolds stress in a plane jet," Exp. Fluids **60**, 1 (2019).

[55] J. R. Khan and S. Rao, "Properties of the turbulent/non-turbulent layer of a turbulent Boussinesq plume: A study using direct numerical simulation," Phys. Fluids **35**, 055140 (2023).

[56] F. T. M. Nieuwstadt, J. Westerweel, and B. J. Boersma, *Turbulence: introduction to theory and applications of turbulent flows* (Springer, 2016).

[57] S. B. Pope, *Turbulent Flows* (Cambridge Univ. Pr., 2000).

[58] J. C. Vassilicos, "Dissipation in turbulent flows," Annu. Rev. Fluid Mech **47**, 95 (2015).

[59] R. R. Taveira and C. B. da Silva, "Kinetic energy budgets near the turbulent/nonturbulent

interface in jets," Phys. Fluids **25**, 015114 (2013).

[60] O. Terashima, Y. Sakai, and K. Nagata, "Simultaneous measurement of all three velocity components and pressure in a plane jet," Meas. Sci. Technol. **25**, 055301 (2014).

[61] T. Watanabe, Y. Sakai, K. Nagata, and Y. Ito, "Large eddy simulation study of turbulent kinetic energy and scalar variance budgets and turbulent/non-turbulent interface in planar jets," Fluid Dyn. Res. **48**, 021407 (2016).

[62] M. J. Lee, J. Kim, and P. Moin, "Structure of turbulence at high shear rate," J. Fluid Mech. **216**, 561 (1990).

[63] K. Takamure, Y. Sakai, Y. Ito, K. Iwano, and T. Hayase, "Dissipation scaling in the transition region of turbulent mixing layer," Int. J. Heat Fluid Flow **75**, 77 (2019).

[64] D. O. Mora, E. Muñiz P., P. Riera T., M. Lagauzere, and M. Obligado, "Energy cascades in active-grid-generated turbulent flows," Phys. Rev. Fluids **4**, 104601 (2019).

[65] Y. Zheng, K. Nagata, and T. Watanabe, "Turbulent characteristics and energy transfer in the far field of active-grid turbulence," Phys. Fluids **33**, 115119 (2021).

[66] T. Watanabe, Y. Sakai, K. Nagata, Y. Ito, and T. Hayase, "Implicit large eddy simulation of a scalar mixing layer in fractal grid turbulence," Phys. Scr. **91**, 074007 (2016).

[67] E. Gutmark and I. Wygnanski, "The planar turbulent jet," J. Fluid Mech. **73**, 465 (1976).

[68] I. Namer and M. V. Ötügen, "Velocity measurements in a plane turbulent air jet at moderate Reynolds numbers," Exp. Fluids **6**, 387 (1988).

[69] S. A. Stanley, S. Sarkar, and J. P. Mellado, "A study of the flow-field evolution and mixing in a planar turbulent jet using direct numerical simulation," J. Fluid Mech. **450**, 377 (2002).

[70] O. Terashima, Y. Sakai, and K. Nagata, "Simultaneous measurement of velocity and pressure in a plane jet," Exp. Fluids **53**, 1149 (2012).

[71] G. A. Freedland, G. Eliason, S. A. Solovitz, and R. B. Cal, "The role of turbulent inflow on the development of a round jet in cross-flow." Int. J. Heat Fluid Flow **84**, 108592 (2020).